crystals

MDPI

Article

Influence of Powder Size on Pore Characteristics and Intermetallic Phase Kinetics in Porous Ti-Al Alloys †

Saif Haider Kayani [1,*], Hafiz Muhammad Salman Ajmal [2], Byung-Joo Kim [1], Nho-Kwang Park [1] and Kwangjun Euh [1,3]

[1] Advanced Metals Division, Korea Institute of Materials Science (KIMS), Changwon 51508, Republic of Korea; kbj@kims.re.kr (B.-J.K.); pnk@kims.re.kr (N.-K.P.); keuh@kims.re.kr (K.E.)
[2] Department of Electrical Engineering, University of Engineering and Technology (Narowal Campus), Lahore 54890, Pakistan; salman.ajmal@uet.edu.pk
[3] Advanced Materials Engineering, Korea University of Science and Technology (UST), Daejeon 34113, Republic of Korea
* Correspondence: saifkayani@kims.re.kr
† This paper is dedicated to the memory of our co-author Nho-Kwang Park.

Abstract: This study investigates the impact of varying powder size on porosity, pore parameters, and intermetallic phase reaction during the reactive sintering of porous TiAl alloys. Ti52Al48 alloys were prepared using coarse (200 mesh) and fine (325 mesh) Ti powders through elemental powder metallurgy and were subsequently sintered at different temperatures, 600 and 1200 °C. Our findings reveal a consistent pore morphology and intermetallic phase microstructure across both alloys. However, samples containing fine Ti powder exhibited a higher number density of small pores compared to those incorporating coarse Ti powders. Additionally, alloys prepared with fine Ti powders demonstrated a higher porosity than those prepared with coarse powders. Consequently, fine Ti powder promoted enhanced diffusion between Ti and Al during sintering, as reflected by the lower onset temperature and enthalpy of intermetallic reaction during sintering.

Keywords: TiAl alloys; powder size; sintering; intermetallic compounds

Citation: Kayani, S.H.; Ajmal, H.M.S.; Kim, B.-J.; Park, N.-K.; Euh, K. Influence of Powder Size on Pore Characteristics and Intermetallic Phase Kinetics in Porous Ti-Al Alloys. *Crystals* **2024**, *14*, 559. https://doi.org/10.3390/cryst14060559

Academic Editor: Benilde F. O. Costa

Received: 10 May 2024
Revised: 6 June 2024
Accepted: 11 June 2024
Published: 17 June 2024

1. Introduction

Porous intermetallic alloys have been considered valuable engineering materials across various industrial sectors, particularly in exhaust gas adsorption and filtration applications [1–4]. However, their utilization in high-temperature exhaust gas filtration has been limited due to inherent susceptibility to corrosion, burning, and oxidation [5–10]. Recently, there has been growing interest in porous TiAl alloys as promising candidates for filtering dust particles from exhaust gases at high temperatures [11,12]. These alloys exhibit exceptional corrosion resistance to both acids and alkalis, along with robust oxidation resistance, even at temperatures exceeding 750 °C [13,14].

Elemental powder metallurgy (EPM) remains a cost-effective method for producing porous TiAl alloys due to its simple sintering process and the use of inexpensive raw materials, i.e., elemental powders [15]. Numerous studies have elucidated the reaction behavior and diffusional phenomenon involved in the formation of porous TiAl alloys [16–18]. For instance, the Kirkendall effect plays a role in the formation of TiAl-based intermetallic compounds (IMCs) [19]. However, the formation of IMCs varies depending on the processing conditions due to disparities in the diffusion rates of Ti and Al [20]. Al particles, with their lower melting point, exhibit rapid diffusion at lower sintering temperatures, migrating towards Ti-rich skeletons and resulting in the formation of Al-rich IMCs [21]. As sintering temperatures increase, the formation of IMCs transition from Al-rich to Ti-rich phases due to the accelerated diffusion of Ti [22]. Consequently, controlling the pore size of the alloy presents a significant challenge owing to the different diffusion behaviors of Ti and Al,

leading to the formation of large pores [23,24]. The presence of these diffusion-controlled coarse pores significantly diminishes the filtration efficacy of porous TiAl alloys, particularly in capturing extremely fine particles. Thus, reducing the pore size of porous TiAl alloys is crucial to enhance their suitability for high-temperature filtration applications.

Cutting-edge manufacturing processes, such as hot-isostatic pressing and spark plasma sintering using alloy powders, have reported the effective development of TiAl alloys with finer pore sizes [25,26]. However, these advanced techniques often lead to a significant increase in production costs, rendering them unsuitable for widespread commercial applications [27,28]. Alternatively, a viable approach to effectively reduce pore size involves decreasing the initial powder size utilized in the EPM process. Previous studies reported that alloys containing smaller powder sizes produce finer pores after the sintering process [29,30]. For instance, Yang et al. [30] demonstrated the fabrication of porous TiAlNb alloys using a combination of powders with varying particle sizes. However, incorporating 2 at. % of Nb yielded a similar pore size as the $Ti_{52}Al_{48}$ (at. %) alloy owing to its lower solubility in Ti [31]. In contrast, Li et al. [32] prepared $TiAl_3$ IMCs of fine pore sizes using fine Al and Ti powders. However, their study was limited to a low-temperature sintering process, specifically at 700 °C. It is well understood that complete IMC formation may not occur during reaction sintering at low temperatures, resulting in a typical skeleton microstructure with Ti-rich cores and $TiAl_3$ formed at the surfaces. Therefore, achieving a well-bonded porous structure necessitates sintering at elevated temperatures. Nevertheless, controlling the melting of fine Al particles during high-temperature sintering presents an utmost challenge. Hence, instead of employing fine Al and Ti powders, in the present study, we aimed to control the pore size of TiAl by utilizing only fine Ti powder. Furthermore, we conducted a comprehensive analysis of the microstructure, the nature of IMCs, and pore parameters of the fabricated alloys after sintering at both low (600 °C) and elevated (1200 °C) temperatures.

2. Materials and Methods

Porous TiAl alloys were fabricated with a nominal composition of 52 at. % Ti and 48 at. % Al using 99.9% Al and hydride–dehydride (HDH) Ti powders obtained from ALCO Engineering, UK, and Sejong Materials Limited, respectively. The Al powder has particle sizes of 600 mesh, while Ti powders of two different mesh sizes (200 and 325) were used. The particle size of powders was conducted using a laser diffraction particle size analyzer (ENSOL instruments, LS I3 320). The powders were dry-blended in a tumbler ball mill for 2 h at a rotational speed of 200 rpm/min under a pure (99.9%) Ar atmosphere. Afterward, the mixed powders were cold-pressed into green compacts with dimensions of 25 mm in width and 5.8 mm in height using a mechanical press (SAMWON-80 ton) under a pressure of 370 MPa. Zinc stearate (1:1 ratio) was utilized as a lubricant for the die walls during compaction. Subsequently, the green compacts were subjected to sintering at the temperatures of 600 and 1200 °C, with a heating rate of 10 °C/min. All sintering processes were conducted under a vacuum of 1×10^{-5} bar, and the samples were maintained at the sintering temperature for 2 h.

Porosity and pore parameters were determined using Mercury inclusion testing (Micromeritics, Autopore IV 9510, Norcross, GA, USA), employing an evacuation pressure of 50 mm/Hg and a 10 s intrusion time. Microstructural analysis was conducted using optical microscopy (OM; Olympus GX50, Tokyo, Japan) and scanning electron microscopy (SEM; Jeol JSM 6610LV, Tokyo, Japan). All microscopy samples underwent grinding and polishing following standard metallography procedures. Intermetallic phase analysis was carried out using an X-ray diffractometer (XRD; Rigaku Dmax 2500, Tokyo, Japan) and energy-dispersive X-ray spectroscopy (EDS) detector integrated with the SEM. The reaction mechanism of intermetallic phases was evaluated using a differential thermal analyzer (DTA; SDT Q6000, New Castle, DE, USA), operated at a heating rate of 10 °C/min. Part of the Ti 200 mesh powder sample results used in this study were taken from the author's previous work [31].

3. Results

3.1. Effect of Powder Size on Microstructure and Bulk Volume

The average particle diameter distribution of the Al 600 mesh and Ti 200 and 325 mesh powders used in this study is depicted in Figure 1a–c, respectively. The analysis revealed an average particle diameter of 20.4 µm for Al 600 mesh, 42.8 µm for Ti 200 mesh, and 26.6 µm for Ti 325 mesh powders.

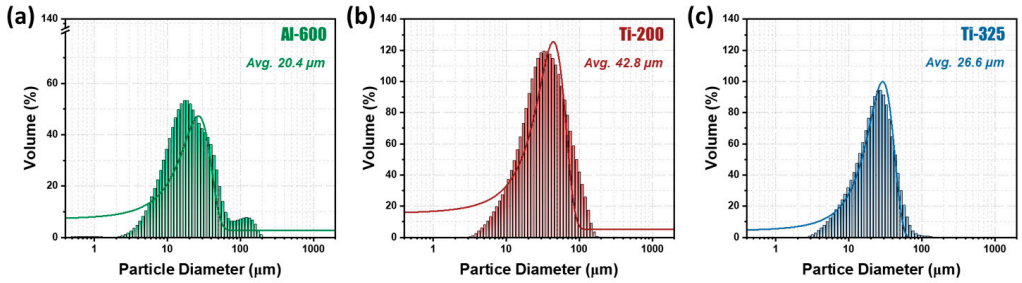

Figure 1. Particle size distribution of powders utilized in the fabrication of $Ti_{52}Al_{48}$ alloys: (**a**) Al 600 mesh, and Ti of (**b**) 200 and (**c**) 325 mesh.

Figure 2 shows secondary electron (SE) images of $Ti_{52}Al_{48}$ alloy specimens prepared to employ (a,c,e) 200 and (b,d,f) 325 mesh Ti powders. Notably, the green compacts present agglomerated powders with small pores resulting from the compaction process. Based on the SE image contrast, dark grey agglomerates were identified as Al, while light grey agglomerates were attributed to Ti. It is discernible that the Ti agglomerates in the 200 mesh sample exhibited a coarser size distribution compared to their 325 mesh counterpart. Consequently, the 200 mesh sample exhibited large inner titanium pores (ITP) as well as inter-particle pores (IPP). Subsequent to sintering at 600 °C, the contrast differentiation within the agglomerates persisted, alongside an escalation in the sizes of ITPs and IPPs. Notably, the 325 mesh Ti powders-containing sample displayed a higher density of smaller pores relative to the 200 mesh specimen. Upon sintering at 1200 °C, both alloys showed a skeleton-type microstructure characterized by large IPPs. The contrast disparity between agglomerates dissipated, indicative of the complete transformation of Ti-rich skeletons into IMCs. However, the IPPs in the 200 mesh sample appeared coarser in comparison to those observed in the 325 mesh specimen.

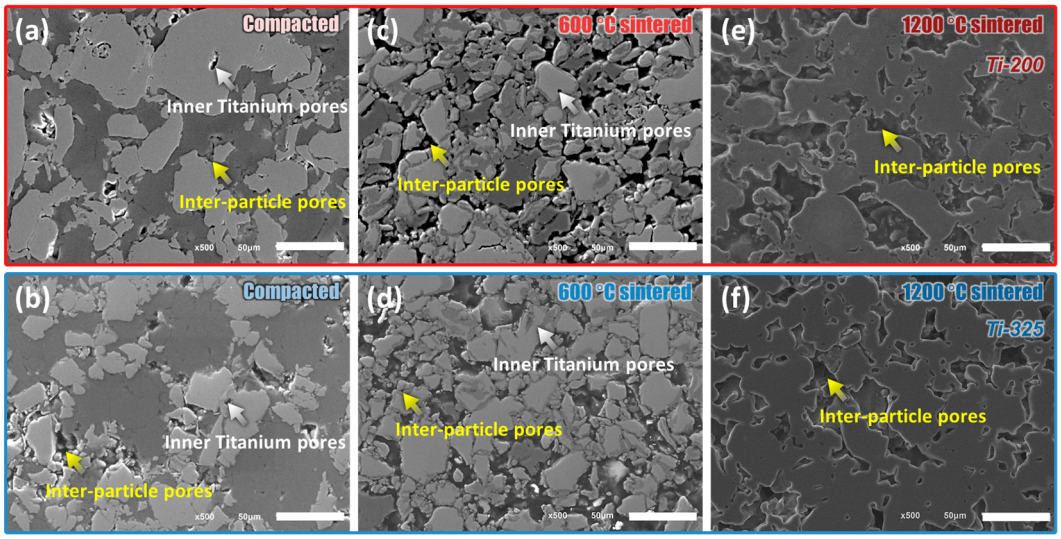

Figure 2. Secondary electron images showing $Ti_{52}Al_{48}$ alloy specimens prepared using Ti powders of varying mesh sizes: (**a**,**c**,**e**) 200 mesh and (**b**,**d**,**f**) 325 mesh samples. (**a**,**b**) Compacted (**c**,**d**) 600 °C, and (**e**,**f**) 1200 °C samples.

3.2. Effect of Powder Size on Pore Size and Porosity

Figure 3 presents the quantitative analysis of pore size and porosity of $Ti_{52}Al_{48}$ alloys, investigated via mercury intrusion tests. Figure 3a,b illustrate the variation in pore diameter for the 200 and 325 mesh samples, respectively. Notably, the pore diameter of the green compacts increased sequentially after sintering, as depicted in Figure 3c for the media pore diameter comparison. According to Table 1, it is evident that the median pore size of the compacted 200 mesh sample increased from 0.70 µm to 3.68 µm and further to 15.28 µm following sintering at 600 and 1200 °C, respectively. Conversely, the 325 mesh sample exhibited a smaller initial pore size of 0.6 µm, which increased to 1.71 µm at 600 °C and to 8.90 µm at 1200 °C, although it remained smaller than the 200 mesh specimen. Figure 3d,e display the cumulative pore volumes of the 200 and 325 mesh alloys, respectively. The corresponding porosity analysis shown in Figure 3f reveals an increase in the porosity of green compacts after sintering. Notably, the porosity of the 325 mesh sample surpassed that of the 200 mesh sample in both compacted and sintered (600 and 1200 °C) states, as presented in Table 1. This increment is attributed to a higher number and density of fine pores in the 325 mesh sample.

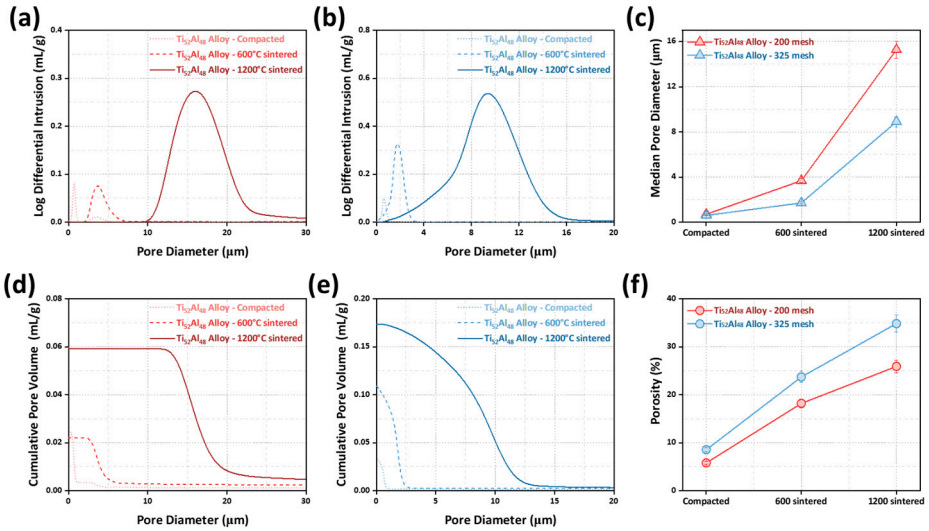

Figure 3. (**a**,**b**) The average pore diameter distributions and (**c**) median pore comparison of $Ti_{52}Al_{48}$ alloy specimens fabricated using Ti powders of different sizes under as-compacted and sintered (600 and 1200 °C) conditions. (**d**,**e**) Cumulative pore volume and (**f**) porosity of alloys for the comparison of $Ti_{52}Al_{48}$ alloy specimens prepared using Ti powders of different sizes under as-compacted and sintered (600 and 1200 °C) conditions. (Part of the 200 mesh sample results were taken from the author's previous work [31]).

Table 1. Pore size parameters of compacted and sintered (600 and 1200 °C) $Ti_{52}Al_{48}$ alloys prepared using Ti powders of different mesh sizes. (Part of the 200 mesh sample results was taken from the author's previous work [31]).

Pore Parameters	200 Mesh			325 Mesh		
	As-Compacted	600 °C Sintered	1200 °C Sintered	As-Compacted	600 °C Sintered	1200 °C Sintered
Median Pore Size (µm)	0.70	3.68	15.28	0.60	1.71	8.90
Porosity (%)	5.82	18.23	25.91	8.51	23.71	34.84

3.3. Effect of Powder Size on Intermetallic Phases

Figure 4a,b present the XRD analysis results for $Ti_{52}Al_{48}$ alloys with Ti powder sizes of 200 and 325 mesh, subjected to compaction and sintering at 600 and 1200 °C. In the

compacted state, both samples displayed distinct peaks corresponding to Ti and Al. To differentiate between the powder sizes of the 200 and 325 mesh specimens, the crystallite size was determined using Scherrer's equation [33]:

$$D = \frac{K\lambda}{\beta\cos\theta} \quad (1)$$

where D represents the crystallite size in nm, K denotes Scherrer's constant (0.9) [33], λ is the wavelength of the X-ray source (0.154 nm), β indicates the full-width at half maximum (in rad), and θ denotes the peak position (in rad). The Ti peak analysis of the as-compacted samples yielded a crystallite size of 0.13 and 0.55 μm for the 200 and 325 mesh samples, respectively. These results suggest that the finer Ti powder particles in the 325 mesh specimen produced smaller agglomerates. After sintering, both samples exhibited no noticeable differences in terms of IMC phase formation. For instance, Al-rich IMCs, $TiAl_3$, and $TiAl_2$ were observed in specimens sintered at 600 °C alongside elemental Ti and Al peaks. The elemental Ti and Al peaks completely disappeared after sintering at 1200 °C, with only Ti-rich IMC peaks observed, i.e., TiAl and Ti_3Al. However, the intensity of the IMC phase peaks in the 325 mesh specimen was significantly higher compared to the 200 mesh specimen. This observation suggests that the diffusion rate is faster in the 325 mesh sample, facilitating more pronounced IMC phase reactions.

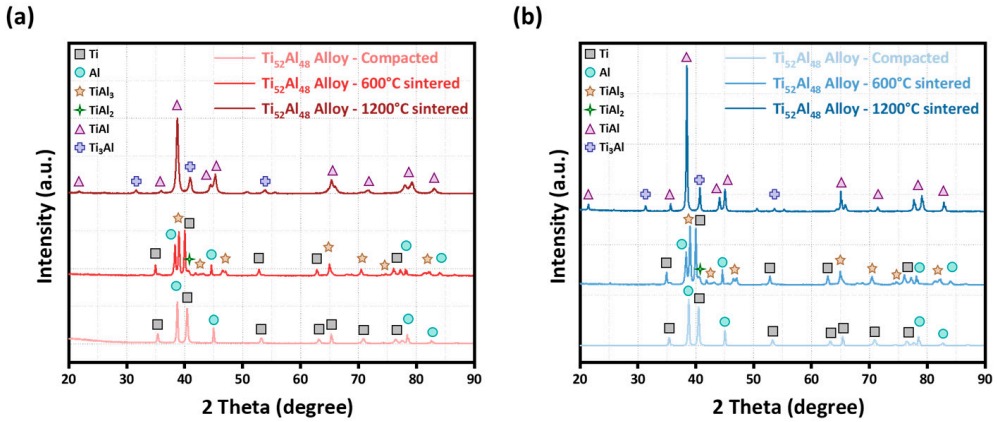

Figure 4. X-ray diffraction analysis of $Ti_{52}Al_{48}$ alloys prepared using Ti powders of varying mesh sizes, (**a**) 200 mesh and (**b**) 325 mesh, under compacted and sintered (600 and 1200 °C) conditions. (Parts of the 200 mesh sample results were taken from the author's previous work [31]).

Furthermore, we conducted backscattered electron (BSE) imaging combined with the EDS analysis of $Ti_{52}Al_{48}$ alloys. Figure 5a–c depicts the BSE images of the 325 mesh specimen in both compacted and sintered states (600 and 1200 °C), respectively. As seen in Figure 5a, the as-compacted sample reveals the presence of Al and Ti agglomerates. Upon sintering at 600 °C, Al-rich IMC Al_3Ti formed on the surface of Ti-rich agglomerates while their core remained rich in Ti. Subsequently, sintering at 1200 °C resulted in the complete transformation of the Ti-rich agglomerates into IMCs. This transformation was evidenced by the presence of the skeleton structure containing the TiAl phase on the surface and the Ti_3Al phase in their cores. The corresponding elemental point analysis results are presented in Table 2.

Table 2. EDS analysis results obtained from the locations shown in Figure 5.

Specimen	As-Compacted		600 °C Sintered		1200 °C Sintered	
Location	Ti	Al	Ti	Al	Ti	Al
i (at. %)	0.70	99.30	99.61	0.39	69.88	30.12
ii (at. %)	99.14	0.86	71.43	28.57	49.53	50.47

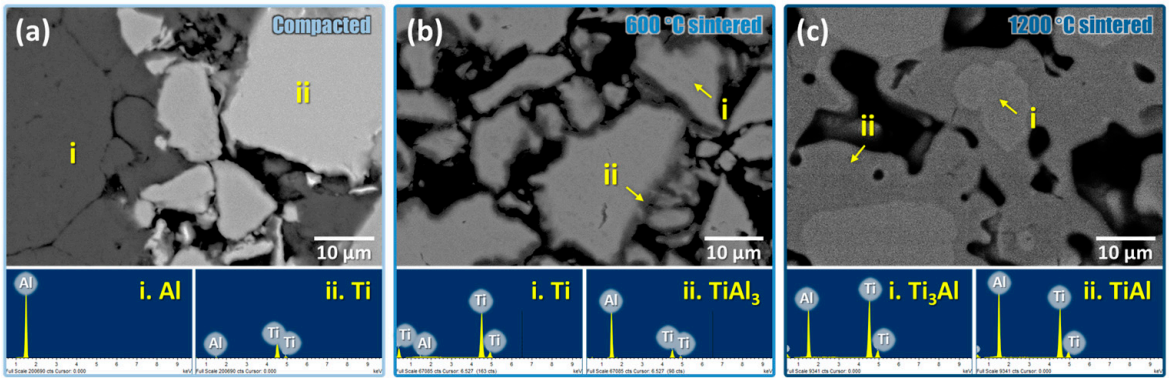

Figure 5. Backscattered electron images of $Ti_{52}Al_{48}$ alloy specimens prepared utilizing 325 mesh Ti powders under (**a**) compacted and sintered (**b**) 600 °C and (**c**) 1200 °C conditions.

4. Discussion

The sintering process of porous TiAl alloys often triggers the formation of IMCs, characterized by an exothermic reaction that induces volume expansion and pore formation. Specifically, due to the higher diffusivity of Al at lower temperatures, a solid–solid diffusion reaction precedes Al melting [34], resulting in the formation of the Al-rich Al_3Ti phase on the surface of Ti agglomerates [35]. This process generates the formation of Kirkendall pores at prior Al sites, which has been explained in detail previously [15]. As the sintering temperature increases, additional intermetallic phase transformations occur via the diffusion of Ti, such as the reactions $TiAl_3 + 2Ti \rightarrow TiAl$ and $TiAl + 2Ti \rightarrow Ti_3Al$. The activation energy for Ti diffusion in the intermetallic structure is significantly higher than that for Al at elevated temperatures [21,22]. Consequently, the presence of excess Ti enhances the thermodynamic stability of Ti-rich IMCs. Moreover, the stoichiometry of the IMCs and the size of the pores may vary depending on the sintering duration at higher temperatures [36,37].

To understand the intermetallic phase reactions in the $Ti_{52}Al_{48}$ alloy, we conducted the DSC analysis on 200 and 325 mesh samples in a compacted state. The DSC results depicted in Figure 6a,b revealed two exothermic peaks and one endothermic peak for both samples. The initial exothermic peak corresponds to the formation of the Al_3Ti phase, succeeded by the endothermic reaction of Al melting [38,39]. Notably, the onset temperature of the first exothermic peak was observed to be lower for the 325 mesh sample (630.1 °C) compared to the 200 mesh sample (638.7 °C). The XRD results presented in Figure 4 corroborate these findings. Furthermore, we calculated the enthalpy of the exothermic reaction for both samples by integrating the area under the peak in the heat flow vs. time plots, as shown in Figure S1. The resulting values of 175.68 kJ/g and 129.77 kJ/g were obtained for the 200 and 325 mesh samples, respectively. Previously, it has been suggested that coarser powders result in less intimate contact between Ti and Al agglomerates, leading to lower interfacial energy and necessitating a stronger diffusion driving force, typically denoted by a higher reaction onset temperature [32,39]. Consequently, the formation of Al_3Ti at elevated temperatures in the samples containing coarser powder releases a larger amount of exothermic heat [32]. The second exothermic peak in the heat flow curves indicates the formation of Ti-rich IMCs following Al melting. Similarly, the peak onset temperature of 325 mesh (806.2 °C) was lower compared to the 200 mesh specimen (810.3 °C). SE images in Figure 2 revealed that Ti agglomerates in the 200 mesh specimen were coarser than those in the 325 mesh sample. Thus, the lower wettability of coarse agglomerates by liquid Al requires prolonged diffusion times for Ti-rich IMC formation, resulting in an increase in the exothermic reaction temperature [40,41].

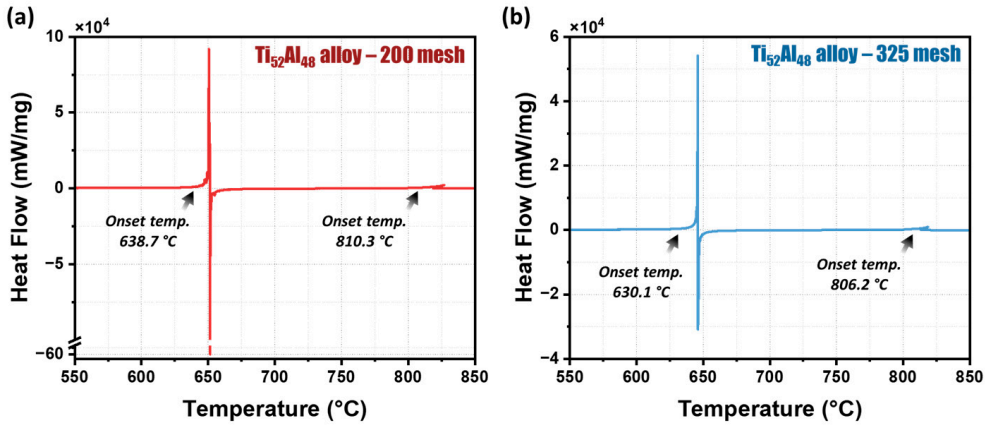

Figure 6. Heat flow curves of $Ti_{52}Al_{48}$ alloys prepared using Ti powders of varying mesh sizes, (**a**) 200 mesh and (**b**) 325 mesh, under compacted and sintered (600 and 1200 °C) conditions.

The driving force for the diffusion of liquid Al is defined by the pressure difference (P) existing between pores originating from compaction and those formed during sintering. Assuming partial melting of all Al agglomerates, the pressure exerted by the liquid Al spreading towards Ti agglomerates can be quantified as follows [32]:

$$P = \frac{2\gamma}{r} \quad (2)$$

where γ represents the surface tension, and r denotes the particle size. Equation (2) elucidates that larger Ti particles result in lower P. Consequently, reaction speeds diminish during sintering in the 200 mesh sample, thereby prolonging diffusion time and facilitating pore enlargement [42]. Conversely, Al diffusion into fine Ti agglomerates is easier, leading to the formation of IMCs with reduced heat flow.

Despite the higher diffusion rates and faster IMC phase reactions observed, the 325 mesh alloy exhibited greater porosity compared to the 200 mesh sample. This increased porosity is attributed to the finer Ti powder particles' higher surface energy [32], which promotes agglomeration. Thus, voids can become trapped within these agglomerates, leading to a higher number and density of pores compared to the coarser Ti powder. This is corroborated by the cumulative pore volume data in Figure 3d,e and the SE images in Figure 2a,b. Additionally, the Kirkendall effect, which involves differential diffusion rates between Ti and Al, can contribute to porosity through the formation of vacancies during sintering [19]. In fine powders, the higher surface area to volume ratio exacerbates this effect, potentially resulting in more pronounced porosity despite the theoretically higher densification rate. Consequently, the 325 mesh samples exhibited a higher density of fine pores with elevated porosity, rendering them favorable for exhaust gas filtration applications.

5. Conclusions

The present study investigated the effect of varying powder sizes on the porosity, pore characteristics, and intermetallic phase formation in porous TiAl alloys. $Ti_{52}Al_{48}$ alloys were fabricated using both fine (325 mesh) and coarse (200 mesh) Ti powders, revealing a skeleton-like IMC microstructure in both cases. At lower sintering temperatures, an Al-rich Al_3Ti phase was formed on the surface of Ti-rich skeletons while the core remained Ti-rich. Upon sintering at 1200 °C, the skeleton cores transformed into the Ti_3Al phase, while the surface exhibited the TiAl phase. Notably, the intermetallic reaction remained consistent across the alloys, with a lower reaction onset temperature and enthalpy observed for the 325 mesh sample. This resulted in the accelerated diffusion of Al into the Ti skeletons at lower temperatures, leading to a high number and density of fine pores and increased porosity in the 325 mesh specimen.

Supplementary Materials: The following supporting information can be downloaded at: https://www.mdpi.com/article/10.3390/cryst14060559/s1, Figure S1: Heat flow vs. time plots of Ti52Al48 alloys prepared using Ti powders of varying mesh sizes; (a) 200 mesh and (b) 325 mesh, under compacted and sintered (600 and 1200 °C) conditions.

Author Contributions: Conceptualization, S.H.K.; methodology, S.H.K.; investigation, S.H.K.; resources, S.H.K.; data curation, S.H.K.; writing—original draft preparation, H.M.S.A. and B.-J.K.; writing—review and editing, H.M.S.A. and B.-J.K.; visualization, N.-K.P.; project administration, supervision, K.E. All authors have read and agreed to the published version of the manuscript.

Funding: This work was financially supported by prime research program of the Korea Institute of materials science (KIMS), and an alliance academic program of Korea University of science and technology (UST), South Korea.

Data Availability Statement: The raw data supporting the conclusions of this article will be made available by the authors on request.

Conflicts of Interest: The authors declare no conflicts of interest.

References

1. Li, X.; Guan, B.Y.; Gao, S.; Lou, X.W.D. A general dual-templating approach to biomass-derived hierarchically porous heteroatom-doped carbon materials for enhanced electrocatalytic oxygen reduction. *Energy Environ. Sci.* **2019**, *12*, 648–655. [CrossRef]
2. Yang, X.-Y.; Chen, L.-H.; Li, Y.; Rooke, J.C.; Sanchez, C.; Su, B.-L. Hierarchically porous materials: Synthesis strategies and structure design. *Chem. Soc. Rev.* **2017**, *46*, 481–558. [CrossRef]
3. Sina, H.; Iyengar, S. Reactive synthesis and characterization of titanium aluminides produced from elemental powder mixtures. *J. Therm. Anal. Calorim.* **2015**, *122*, 689–698. [CrossRef]
4. Jiang, Y.; Deng, C.; He, Y.; Zhao, Y.; Xu, N.; Zou, J.; Huang, B.; Liu, C.T. Reactive synthesis of microporous titanium-aluminide membranes. *Mater. Lett.* **2009**, *63*, 22–24. [CrossRef]
5. Shi, Q.; Qin, B.; Feng, P.; Ran, H.; Song, B.; Wang, J.; Ge, Y. Synthesis, microstructure and properties of Ti–Al porous intermetallic compounds prepared by a thermal explosion reaction. *RSC Adv.* **2015**, *5*, 46339–46347. [CrossRef]
6. Sun, M.-H.; Huang, S.-Z.; Chen, L.-H.; Li, Y.; Yang, X.-Y.; Yuan, Z.-Y.; Su, B.-L. Applications of hierarchically structured porous materials from energy storage and conversion, catalysis, photocatalysis, adsorption, separation, and sensing to biomedicine. *Chem. Soc. Rev.* **2016**, *45*, 3479–3563. [CrossRef]
7. Zhang, G.-H.; Zhu, Q.-H.; Zhang, L.; Yong, F.; Zhang, Z.; Wang, S.-L.; Wang, Y.; He, L.; Tao, G.-H. High-performance particulate matter including nanoscale particle removal by a self-powered air filter. *Nat. Commun.* **2020**, *11*, 1653. [CrossRef]
8. Sharma, P.; Yadav, P.; Ghosh, C.; Singh, B. Heavy metal capture from the suspended particulate matter by Morus alba and evidence of foliar uptake and translocation of PM associated zinc using radiotracer (65Zn). *Chemosphere* **2020**, *254*, 126863. [CrossRef] [PubMed]
9. Petriev, I.; Pushankina, P.; Bolotin, S.; Lutsenko, I.; Kukueva, E.; Baryshev, M. The influence of modifying nanoflower and nanostar type Pd coatings on low temperature hydrogen permeability through Pd-containing membranes. *J. Membr. Sci.* **2021**, *620*, 118894. [CrossRef]
10. Aydoğmuş, T.; Palani, D.K.H.; Kelen, F. Processing of porous β-type Ti74Nb26 alloys for biomedical applications. *J. Alloys Compd.* **2021**, *872*, 159737. [CrossRef]
11. Cobbinah, P.V.; Matizamhuka, W.; Machaka, R.; Shongwe, M.B.; Yamabe-Mitarai, Y. The effect of Ta additions on the oxidation resistance of SPS-produced TiAl alloys. *Int. J. Adv. Manuf. Technol.* **2020**, *106*, 3203–3215. [CrossRef]
12. Cai, X.; Bo, X.; Feng, P.; Ren, X.; Kang, X.; Xu, C.; Zhang, P. Porous NbAl3/$TiAl_3$ intermetallic composites with controllable porosity and pore morphology prepared by two-step thermal explosion. *J. Mater. Res. Technol.* **2019**, *8*, 3188–3197. [CrossRef]
13. Kothari, K.; Radhakrishnan, R.; Wereley, N.M. Advances in gamma titanium aluminides and their manufacturing techniques. *Prog. Aerosp. Sci.* **2012**, *55*, 1–16. [CrossRef]
14. Jiang, Y.; He, Y.H.; Xu, N.P.; Zou, J.; Huang, B.Y.; Liu, C.T. Effects of the Al content on pore structures of porous Ti–Al alloys. *Intermetallics* **2008**, *16*, 327–332. [CrossRef]
15. Kayani, S.H.; Cui, M.; Ahmed, R.T.M.; Cho, Y.-H.; Lee, J.-M.; Park, N.-K.; Ajmal, H.M.S.; Euh, K. Pore formation mechanism and intermetallic phase transformation in Ti–Al alloy during reactive sintering. *J. Mater. Res. Technol.* **2023**, *22*, 1878–1887. [CrossRef]
16. Wang, Y.H.; Lin, J.P.; He, Y.H.; Wang, Y.L.; Chen, G.L. Effect of Nb on pore structure and tensile property of Ti–48Al cellular alloy. *J. Alloys Compd.* **2008**, *456*, 297–303. [CrossRef]
17. Meng, X.L.; Cai, W.; Lau, K.T.; Zhao, L.C.; Zhou, L.M. Phase transformation and microstructure of quaternary TiNiHfCu high temperature shape memory alloys. *Intermetallics* **2005**, *13*, 197–201. [CrossRef]
18. Ma, Y.; Fan, Q.; Zhang, J.; Shi, J.; Xiao, G.; Gu, M. Microstructural evolution during self-propagating high-temperature synthesis of Ti-Al system. *J. Wuhan Univ. Technol.-Mater Sci. Ed.* **2008**, *23*, 381–385. [CrossRef]
19. He, Y.H.; Jiang, Y.; Xu, N.P.; Zou, J.; Huang, B.Y.; Liu, C.T.; Liaw, P.K. Fabrication of Ti–Al Micro/ Nanometer-Sized Porous Alloys through the Kirkendall Effect. *Adv. Mater.* **2007**, *19*, 2102–2106. [CrossRef]

20. Mishin, Y.; Herzig, C. Diffusion in the Ti–Al system. *Acta Mater.* **2000**, *48*, 589–623. [CrossRef]
21. Gupta, R.K.; Pant, B.; Agarwala, V.; Sinha, P.P. Differential scanning calorimetry and reaction kinetics studies of γ + α2 Ti aluminide. *Mater. Chem. Phys.* **2012**, *137*, 483–492. [CrossRef]
22. Herzig, C.; Przeorski, T.; Mishin, Y. Self-diffusion in γ-TiAl: An experimental study and atomistic calculations. *Intermetallics* **1999**, *7*, 389–404. [CrossRef]
23. Mackowiak, J.; Shreir, L.L. The nature and growth of interaction layers formed during the reaction between solid titanium and liquid aluminium. *J. Less Common Met.* **1959**, *1*, 456–466. [CrossRef]
24. Sohn, H.Y.; Wang, X. Mathematical and experimental investigation of the self-propagating high-temperature synthesis (SHS) of $TiAl_3$ and Ni3Al intermetallic compounds. *J. Mater. Sci.* **1996**, *31*, 3281–3288. [CrossRef]
25. Mphahlele, M.R.; Olubambi, P.A.; Olevsky, E.A. Advances in Sintering of Titanium Aluminide: A Review. *JOM* **2023**, *75*, 2877–2896. [CrossRef]
26. Karunanithi, R.; Prashanth, M.; Kamaraj, M.; Sivasankaran, S.; Kumaraswamidhas, L.A.; Alhomidan, A.A. Synthesis, characterization, and mechanical behavior of ultra-fine-grained Ti-6Al-5V alloy prepared by mechanical alloying and spark plasma sintering. *Mater. Today Commun.* **2024**, *38*, 108228. [CrossRef]
27. Gerling, R.; Clemens, H.; Schimansky, F.P. Powder Metallurgical Processing of Intermetallic Gamma Titanium Aluminides. *Adv. Eng. Mater.* **2004**, *6*, 23–38. [CrossRef]
28. Gao, H.Y.; He, Y.H.; Shen, P.Z.; Jiang, Y.; Liu, C.T. Effect of pressure on pore structure of porous FeAl intermetallics. *Adv. Powder Technol.* **2015**, *26*, 882–886. [CrossRef]
29. Liang, Y.; Yang, F.; Zhang, L.; Lin, J.; Shang, S.; Liu, Z.-K. Reaction behavior and pore formation mechanism of TiAl–Nb porous alloys prepared by elemental powder metallurgy. *Intermetallics* **2014**, *44*, 1–7. [CrossRef]
30. Yang, F.; Zhang, L.; Lin, J.; Liang, Y.; He, Y.; Shang, S.; Liu, Z.-K. Pore structure and gas permeability of high Nb-containing TiAl porous alloys by elemental powder metallurgy for microfiltration application. *Intermetallics* **2013**, *33*, 2–7. [CrossRef]
31. Kayani, S.H.; Park, N.-K. Effect of Cr and Nb on the phase transformation and pore formation of Ti-Al base alloys. *J. Alloys Compd.* **2017**, *708*, 308–315. [CrossRef]
32. Li, K.; Zhang, T.; Zhu, Y. Reaction Behavior of Porous $TiAl_3$ Intermetallics Fabricated by Thermal Explosion with Different Particle Sizes. *Materials* **2021**, *14*, 7417. [CrossRef] [PubMed]
33. Liu, Y.; Zhang, W.; Peng, Y.; Fan, G.; Liu, B. Effects of TiAl Alloy as a Binder on Cubic Boron Nitride Composites. *Materials* **2021**, *14*, 6335. [CrossRef]
34. Sienkiewicz, J.; Kuroda, S.; Molak, R.M.; Murakami, H.; Araki, H.; Takamori, S.; Kurzydłowski, K.J. Fabrication of TiAl intermetallic phases by heat treatment of warm sprayed metal precursors. *Intermetallics* **2014**, *49*, 57–64. [CrossRef]
35. Wang, T.; Lu, Y.X.; Zhu, M.L.; Zhang, J.S.; Ji, S.J. DSC Research on Critical Temperature in Thermal Explosion Synthesis Reaction $Ti+_3Al \rightarrow TiAl_3$. *J. Therm. Anal. Calorim.* **2002**, *67*, 605–611. [CrossRef]
36. Školáková, A.; Leitner, J.; Salvetr, P.; Novák, P.; Deduytsche, D.; Kopeček, J.; Detavernier, C.; Vojtěch, D. Kinetic and thermodynamic description of intermediary phases formation in Ti-Al system during reactive sintering. *Mater. Chem. Phys.* **2019**, *230*, 122–130. [CrossRef]
37. Sujata, M.; Bhargava, S.; Sangal, S. On the formation of $TiAl_3$ during reaction between solid Ti and liquid Al. *J. Mater. Sci. Lett.* **1997**, *16*, 1175–1178. [CrossRef]
38. Jiao, X.; Wang, X.; Feng, P.; Liu, Y.; Zhang, L.; Akhtar, F. Microstructure Evolution and Pore Formation Mechanism of Porous $TiAl_3$ Intermetallics via Reactive Sintering. *Acta Metall. Sin. Engl. Lett.* **2018**, *31*, 440–448. [CrossRef]
39. Jiao, X.; Ren, X.; Feng, P. Visible Observation and Formation Mechanism of Porous $TiAl_3$ Intermetallics During the Continuous Sintering Process. *JOM* **2020**, *72*, 3652–3660. [CrossRef]
40. Ye, S.; Hao, H.; Mo, W.; Yu, K.; Liu, L.; Deng, C.; Yu, P. Effects of cold compacting pressure on the expansion behavior of Ti-48Al during sintering. *J. Alloys Compd.* **2016**, *673*, 399–404. [CrossRef]
41. Che, H.Q.; Fan, Q.C. Microstructural evolution during the ignition/quenching of pre-heated Ti/3Al powders. *J. Alloys Compd.* **2009**, *475*, 184–190. [CrossRef]
42. Jiang, Y.; He, Y.; Liu, C.T. Review of porous intermetallic compounds by reactive synthesis of elemental powders. *Intermetallics* **2018**, *93*, 217–226. [CrossRef]